Cell

Switch between Large Hand-Over-Hand and Small Inchworm-like Steps in Myosin VI

So Nishikawa,[1,6] Ikuo Arimoto,[1,6] Keigo Ikezaki,[1,6] Mitsuhiro Sugawa,[1] Hiroshi Ueno,[2] Tomotaka Komori,[1] Atsuko H. Iwane,[1] and Toshio Yanagida[1,3,4,5,*]

[1]Graduate School of Frontier Biosciences, Osaka University, Yamadaoka, Suita, Osaka, 565-0871, Japan
[2]Institute of Scientific and Industrial Research, Osaka University, Mihogaoka, Ibaraki, Osaka, 567-0047, Japan
[3]WPI, Immunology Frontier Research Center, Osaka University, Yamadaoka, Suita, Osaka, 565-0871, Japan
[4]RIKEN, Yamadaoka, Suita, Osaka, 565-0871, Japan
[5]National Institute of Information and Communication Technology, Nukuikitamachi, Koganei, Tokyo, 184-8795, Japan
[6]These authors contributed equally to this work
*Correspondence: yanagida@phys1.med.osaka-u.ac.jp
DOI 10.1016/j.cell.2010.08.033

SUMMARY

Many biological motor molecules move within cells using stepsizes predictable from their structures. Myosin VI, however, has much larger and more broadly distributed stepsizes than those predicted from its short lever arms. We explain the discrepancy by monitoring Qdots and gold nanoparticles attached to the myosin-VI motor domains using high-sensitivity nanoimaging. The large stepsizes were attributed to an extended and relatively rigid lever arm; their variability to two stepsizes, one large (72 nm) and one small (44 nm). These results suggest that there exist two tilt angles during myosin-VI stepping, which correspond to the pre- and postpowerstroke states and regulate the leading head. The large steps are consistent with the previously reported hand-over-hand mechanism, while the small steps follow an inchworm-like mechanism and increase in frequency with ADP. Switching between these two mechanisms in a strain-sensitive, ADP-dependent manner allows myosin VI to fulfill its multiple cellular tasks including vesicle transport and membrane anchoring.

INTRODUCTION

Myosin VI is a universal motor protein that has been identified in organisms ranging from the roundworm *Caenorhabditis elegans* to humans. It is responsible for many cellular functions including endocytosis, protein secretion, and maintenance of both the Golgi morphology and stereocilia (reviewed in Sweeney and Houdusse, 2007). The myosin VI heavy chain, like many other myosins, consists of two domains, the head and tail. The head is composed of an N-terminal motor domain that consists of a catalytic domain, which includes the actin and nucleotide binding sites, a converter region, and a lever arm that includes two calmodulin-binding motifs (unique insert and IQ motif) (Bahloul et al., 2004). The tail is composed of four subdomains: the proximal, medial and distal tails, and the C-terminal cargo-binding domain. It is also the location where the two heads adjoin to form a dimer, which is the state in which myosin VI inherently functions in cells (Altman et al., 2007; Park et al., 2006; Phichith et al., 2009). While the crystal structure of the head has been solved, the structure of most of the tail remains unknown (Menetrey et al., 2005, 2008).

As a dimer, myosin VI is a processive motor that moves in a direction opposite that of most other myosins (Bryant et al., 2007; Nishikawa et al., 2002; Park et al., 2007; Rock et al., 2001; Wells et al., 1999). It has short lever arms that include two calmodulin binding motifs and moves processively along actin helical pitches with large step sizes (60–70 nm) (Okten et al., 2004; Park et al., 2006; Yildiz et al., 2004) that are comparable to myosin V despite the latter having much longer lever arms (six calmodulin binding motifs) (Yildiz et al., 2003). In general, the myosin VI stepsize is difficult to reconcile when considering its short lever arms (Spudich and Sivaramakrishnan, 2010). Most likely, either myosin VI uses an alternative mechanism from the conventional lever arm model, a model frequently applied to other myosins, or its tail domain acts as an extended lever arm. Along with its unexpectedly long stepsize, myosin VI is also distinct in that its step sizes are highly variable (Lan and Sun, 2006; Rock et al., 2001; Sun et al., 2007; Yildiz et al., 2004).

Recently, Spink et al. and Sivaramakrishnan and Spudich have proposed that myosin VI forms a dimer at the cargo binding domain and that its medial tail is a stable α-helix that can act as a relatively rigid extended lever arm (Sivaramakrishnan and Spudich, 2009; Spink et al., 2008). On the other hand, Mukherjea et al. have argued that myosin VI forms its dimer at its proximal and medial tails, the latter consisting of a three-helix bundle in the monomeric state that upon dimerization subsequently pulls the helix junction to unfold and cause the lever arm to extend in a somewhat flexible manner (Mukherjea et al., 2009). The two models have conflicting limitations. If the extended lever

arm is rigid, then the large stepsize can be explained but the broad distribution of stepsizes cannot. In contrast, if the unfolded three-helix bundle is relatively flexible, then the broad distribution of stepsizes can be accounted for but the large stepsizes over a wide range of loads are not (Altman et al., 2004).

Here, to further investigate myosin VI's distinctive step behavior, we observed myosin VI steps by monitoring quantum dots (Qdots) and gold nanoparticles (GNPs) attached directly to the motor domain, as these offer better spatial and temporal resolutions during single molecule tracking compared to GFP (Balci et al., 2005; Nishikawa et al., 2002; Yildiz et al., 2004). Other groups have used organic fluorescent dyes like Cy3 or Cy5, but attached them to calmodulin bound to an IQ motif, i.e., the lever arm (Okten et al., 2004; Yildiz et al., 2004). Since in these studies the IQ motif is at the distal end of the head, far from the actin binding site, the relative position of the head to the actin filament could not be ascertained. Along with modifying the labeling molecule, we improved the spatial and temporal resolutions of single molecule nanoimaging by using total internal reflection fluorescence microscopy (TIRFM) and total internal reflection dark field microscopy (TIRDFM). Using these methods, we found two distinct stepsizes, one large (72 nm) and one small (44 nm), and the existence of two tilt angles during myosin-VI stepping. The large steps are consistent with the previously reported hand-over-hand mechanism, while the small steps follow an inchworm-like mechanism and increase in frequency with ADP. Switching between these two mechanisms is likely to allow myosin VI to fulfill its multiple cellular tasks including vesicle transport and membrane anchoring.

RESULTS

Large and Small Steps by Myosin-VI Heads

Myosin VI was labeled with Qdot 525 at its N terminus, which is the location of the head (Figure 1A). We observed Qdots by TIRFM (Funatsu et al., 1995; Tokunaga et al., 1997; Vale et al., 1996) with some modification to achieve 2 nm spatial and 0.1 s temporal resolutions (Experimental Procedures, Extended Experimental Procedures, and Figure S1A available online, Yildiz et al., 2003). Figures 1B and 1C show the time trajectories of steps by single-labeled myosin VI heads in the presence of ATP without and with ADP, respectively. The head underwent mostly forward steps, although some backward steps were observed. The forward step size had a large size distribution, consistent with previous studies (Okten et al., 2004; Park et al., 2006; Yildiz et al., 2004). However, within this large distribution emerged the appearance of two distinct types of forward steps, one small (44 nm) and one large (72 nm). Backward steps of –42 nm were also seen. All step sizes were independent of ATP concentrations ranging from 20 μM to 1 mM (Figures 2A–2D). The standard deviations of small forward, large forward and backward step size distributions were ±7 nm, ±9 nm, and ±7 nm, respectively, all of which are similar to those (±7 nm) of Qdot labeled myosin V, a myosin that has a long, rigid lever arm and takes large forward steps.

To exclude the possibility that steric hindrance generated from the attached Qdot was responsible for the small steps, we examined tetramethyl rhodamine (TMR) labeled myosin VI as a reference. The velocity and run length for Qdot labeled myosin VI were consistent with those for TMR labeled myosin VI (Table S1). Furthermore small (44 nm) steps were also resolved for TMR labeled myosin VI at low ATP concentration (Figure S2). These results indicate that steric hindrance due to Qdot labeling at the head is not significant.

When 100 μM ADP was added to 20 μM ATP, the fraction of small forward steps became the majority (Figure 1C and Figure 2B). Such an effect by ADP was also observed in the presence of high (1 mM) ATP, although to a lesser degree (Figures 2C and 2D). Overall, the stepping frequency ratio for large and small forward steps and small backward steps was 1: 0.4: 0.1 at 0 μM

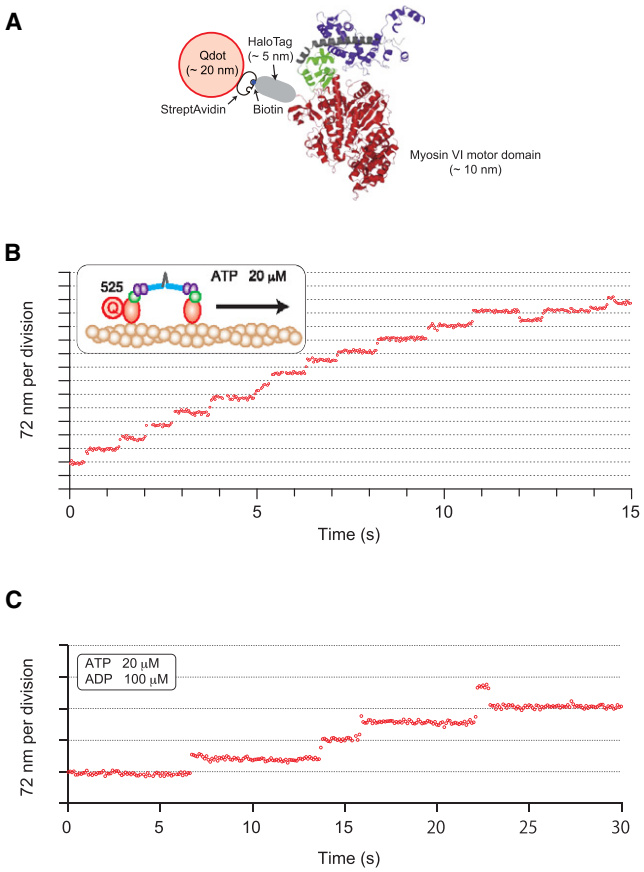

Figure 1. Stepping Behavior of a Myosin-VI Head Labeled with a Qdot

(A) Cartoon illustrating a Qdot labeled myosin VI head. The myosin VI head (Menetrey, et al., PDB: 2BKI) was labeled at the N terminus via a HaloTag domain (~5 nm). The catalytic domain, converter domain, calmodulin binding (lever arm) domain, and two calmodulins are shown as red, green, black and purple, respectively. A Qdot (~20 nm in diameter) was attached to the Halotag via a biotin and streptavidin system. Image is not to scale.

(B) Time trajectory of steps by a myosin VI head labeled with a Qdot525. Steps were observed at 20 μM ATP in assay buffer (20 mM HEPES-KOH, pH7.8, 25 mM KCl, 5 mM $MgCl_2$, and 1 mM EGTA) plus an oxygen scavenger system (Harada, et al., 1990). Qdot525 were visualized using custom made TIRFM (Figure S1A).

(C) Time trajectory of steps at 20 μM ATP and 100 μM ADP in assay buffer plus an oxygen scavenger system.

Experiments were done at room temperature (27°C).

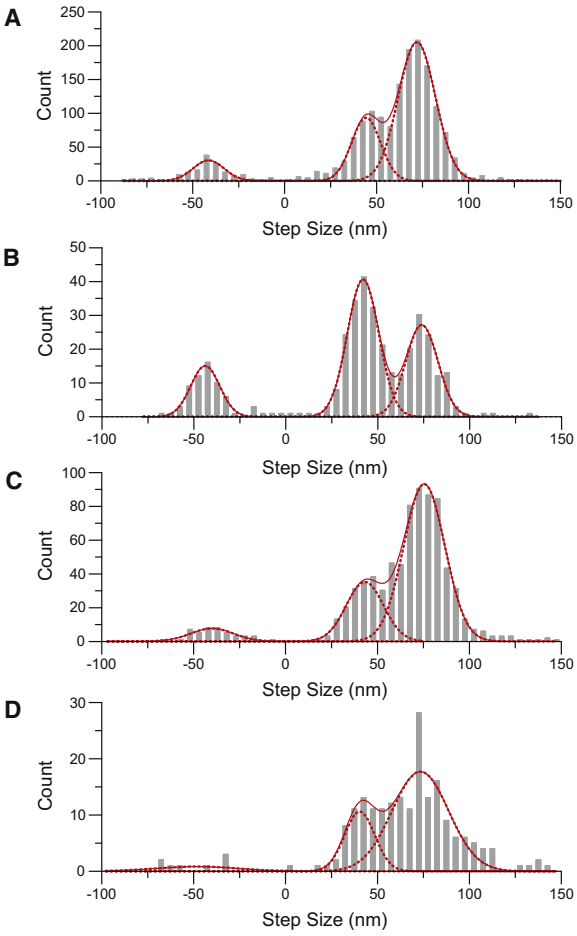

Figure 2. Stepsize Distribution of a Myosin-VI Head

(A) Histogram of stepsizes at 20 μM ATP. The histogram of stepsizes was best fit to a three Gaussian function using a least-squares method (solid and broken lines) with peaks at 71.9 ± 8.9 nm, 43.6 ± 6.9 nm and –41.5 ± 7.0 nm. The number of observed steps was 1256.

(B) Effect of ADP on steps at 20 μM ATP. The distribution of steps when the ATP regenerating system was replaced with 100 μM ADP at 20 μM ATP. The peak positions of a three Gaussian function fit were 73.9 ± 8.7 nm, 42.0 ± 8.6 nm and –43.8 ± 7.9 nm. The number of observed steps was 297.

(C) Histogram of steps at 1020 μM ATP. The histogram was best fit to a three Gaussian function using a least-squares method (solid and broken lines) with peaks at 75.3 ± 9.6 nm, 42.9 ± 8.6 nm and –40.5 ± 9.9 nm. The number of observed steps was 762.

(D) Effect of ADP on the steps at 1020 μM ATP. The histogram shows the distribution of steps when the concentration of ATP was 1020 μM and the ATP regenerating system was replaced with 100 μM ADP. The peak positions of the three Gaussian function fit were 73.4 ± 12.7 nm, 40.4 ± 6.7 nm and - 47.9 ± 18.6 nm. The number of observed steps was 199.

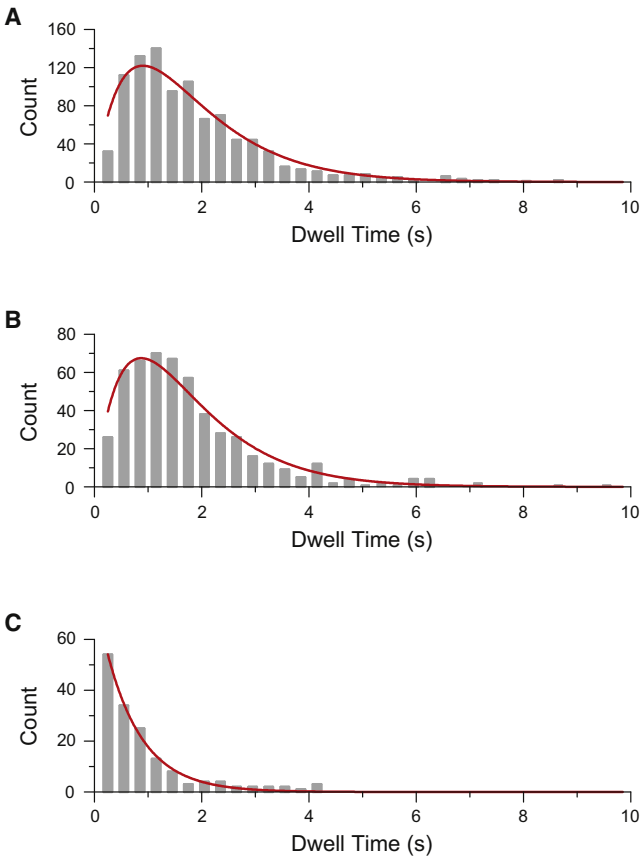

Figure 3. Dwell Time of Steps by a Myosin-VI Head

(A and B) Histograms of dwell times just before forward large (60–150 nm) and small (0–60 nm) steps, respectively. The histograms were best fit by a convolution of two exponentials (tk^2 exp (-kt)), each having the same rate constant, k. The value of k for large and small steps was 1.1 s^{-1} at 20 μM ATP.

(C) Histogram of dwell times just before backward steps. The histogram was best fit by a single exponential with a rate constant of 1.5 s^{-1} at 20 μM ATP.

ADP and 20 μM ATP (Figure 2A), and 1: 1.5: 0.5 at 100 μM ADP and 20 μM ATP (Figure 2B). Thus, the numbers of small forward and backward steps that increased in response to ADP were 1.1 and 0.4, normalized by the number of forward large steps, respectively. These results indicate that ADP had a pronounced effect on the small forward step frequency and a slight one on the backward step frequency. The slight increase in backward step frequency can be explained as follows. ADP competes with ATP for binding at the rear head, while at sufficiently high ADP/ATP ratios, the relative rates of ATP binding to the rear and leading heads become similar. ATP binding to the leading head promotes detachment, which subsequently increases the probability of backward steps.

In order to investigate the stepping manner, the dwell times of forward and backward steps by labeled heads were analyzed. The histograms of dwell times just before the large (60–150 nm) (Figure 3A) and small (0–60 nm) (Figure 3B) forward steps were fit to a convolution of two exponentials (tk^2 exp [-kt]), each having the same rate constant, k. This is reasonable if we assume that labeled and nonlabeled myosin VI heads alternate steps, each corresponding to a single chemical cycle of ATPase. The rate constant k changed with ATP concentration. The ADP dissociation rate was 4.4 s^{-1}, while the ATP association rate was 0.037 $\mu M^{-1}s^{-1}$, both of which are consistent with previous studies that failed to distinguish small and large steps, meaning those observed values were likely averages of the two (De La Cruz et al., 2001; Yildiz et al., 2004). Furthermore, these

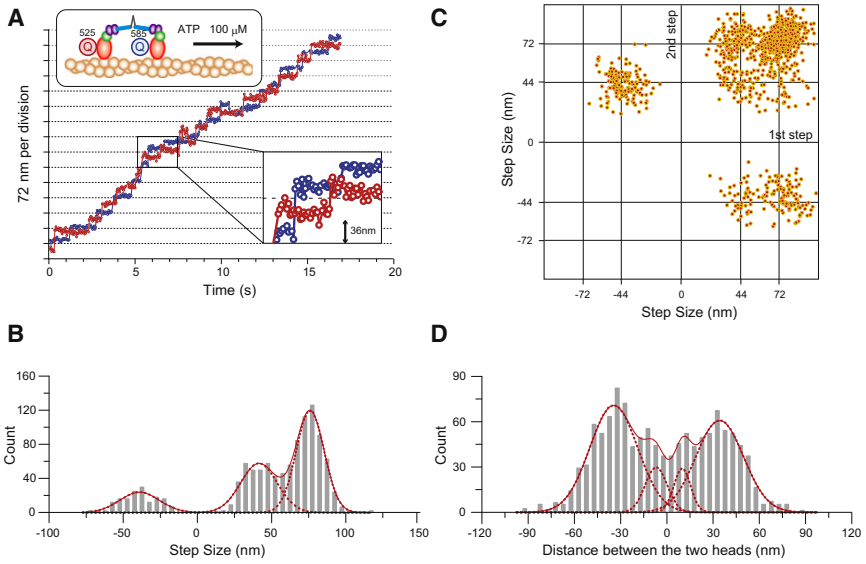

Figure 4. Simultaneous Observation of Steps by Both Myosin-VI Heads

(A) Time trajectory of steps by two myosin VI heads. The two heads were labeled with Qdot525 (red) and Qdot585 (blue), respectively, at 100 μM ATP. The positions of the Qdots are plotted. Insertion, small steps on an expanded time scale.

(B) Stepsizes by two heads. The histogram was best fit to a three Gaussian function using a least-squares method (red solid and broken lines) with peaks of 75.6 ± 7.8 nm, 41.0 ± 10.2 nm and − 39.6 ± 11.0 nm.

(C) The correlation between two successive steps (n = 1075). Step size was measured using SHREC observations, meaning all steps, not just those by one head, were observed.

(D) Distances between the positions of the two heads after steps were completed at 100 μM ATP. The histogram was best fit to a four Gaussian function using a least-squares method (solid and broken red lines) with peaks at +34.3 ± 12.8, +9.9 ± 4.3, −34.5 ± 12.9, and −6.9 ± 5.8 nm. The number of observed steps was 1219.

results also demonstrate Qdot labeling created negligible steric hindrance on myosin-VI motility.

On the other hand, the histogram of dwell times just before backward steps by head-labeled myosin VI fits a single time constant and matches the rate of forward steps at different ATP concentrations (Figure 3C). This suggests that backward steps are due to detachment of the leading head from actin by ATP binding or spontaneous detachment of the leading head without ATP binding.

Simultaneously Observing Two Myosin-VI Heads Reveals Stepping Pattern of Large and Small Steps

Next, in order to clarify how the small and large steps are generated by the two myosin-VI heads, we traced steps by the two heads simultaneously by monitoring differentially-labeled heads with Qdots of different emission spectra using the SHREC method (Churchman et al., 2005). Similar to our concerns above, to exclude the possibility that double Qdot labeling disturbed myosin VI motility, we compared its velocity and run length with those of TMR labeled myosin VI (Table S1), finding them to be the same.

Figure 4A shows the time trajectories of the head position. Each head underwent forward (large, 76 ± 9 nm; small, 41 ± 12 nm) and backward steps (−40 ± 13 nm) (Figure 4B), similar to the profile seen for single labeled heads (Figure 2A). The large forward steps were processive and alternated between the two heads, consistent with the hand-over-hand mechanism (Yildiz et al., 2003). Small steps were also processive, but could not be explained by the hand-over-hand mechanism. For these, the trailing head first underwent a small forward step and bound to the actin filament at a location immediately adjacent to the leading head (Figure 4A, insertion). Then either head (mostly the original leading head) underwent a small forward step. No backward steps (out of 280 observations) were observed from the adjacent head binding state. To clarify the correlation of large, small and backward steps, we analyzed the relationship of two successive steps. Figure 4C shows seven densities in a correlation pattern (pattern I: successive 72 nm and 72 nm steps; pattern II: 72 nm and 44 nm steps; pattern III: 44 nm and 72 nm steps; pattern IV: 44 nm and 44 nm steps; pattern V: 72 nm and −44 nm steps; pattern VI: 44 nm and −44 nm steps; and pattern VII: −44 nm and 44 nm steps). A striking feature in this figure is that there is no density for successive backward steps; backward steps are always followed by small forward steps.

Figure 4D shows a histogram of distances between the two heads after a step was completed. Distance represents the distance between the original leading head and original trailing head such that when the original trailing head leads, distance is negative. The histogram fit to a four Gaussian function with peaks of +35, +10, −7 and −34 nm. The +35 and −34 nm values are consistent with the heads spanning the actin half helical pitch (36 nm), while in myosin V, only a 36 nm distance between the two heads was reported using Qdot labeled myosin V (Warshaw et al., 2005). The +10 and −7 nm values are consistent with the heads being adjacent to each other (adjacent head binding state). The fraction of adjacent head binding state increased in the presence of ADP (data not shown). The feature deduced from the histogram fit to a four Gaussian function is inconsistent with a simplified hand-over-hand model deduced from a histogram fit to a single Gaussian function (Balci et al., 2005). One possible explanation for the disagreeing results is the labels used to determine distance. In the Balci report, eGFP was used. We, however, labeled with Qdot, which is much brighter than eGFP and therefore may explain why we saw two peaks in the two heads distance distribution.

Furthermore, we analyzed the step size distribution after heads took the adjacent binding state (heads separated by less than 15 nm; Figure S4A) and that after taking the distant binding state (heads separated by over 30 nm; Figure S4B). Myosin VI produced only small forward steps (45 nm) after the adjacent binding state (Figure S4A), but took large (75 nm), small

(40 nm) and backward (−43 nm) steps at a 1:0.2:0.3 ratio after the distant binding state (Figure S4B).

First Substep before Brownian Search Regulates Myosin-VI Step Size

It has been reported that myosin-V stepping is determined largely by a deterministic power stroke with a minor contribution from a diffusive search. This is thought to explain myosin V's narrow step size distribution. Analogously, myosin-VI stepping is thought to have a much larger diffusive search component because of its short lever arm and broad step size distribution (Ali et al., 2004; Altman et al., 2004; Lan and Sun, 2006; Okten et al., 2004; Rock et al., 2005; Sun et al., 2007). Dunn and Spudich shed light on this matter for myosin V by achieving a temporal resolution of 320 μs (3125 frames/s) using dark field imaging and gold nanoparticles (GNPs), which allowed them to report an elusive intermediate state (Dunn and Spudich, 2007). This state describes how the unbound head freely diffuses and searches for the forward binding site (Brownian search) (Dunn and Spudich, 2007; Shiroguchi and Kinosita, 2007). Thus, to understand the role of the Brownian search mechanism, we constructed TIR (total internal reflection) based dark-field illumination geometry by using a perforated mirror and a complementary metal oxide semiconductor (Ueno et al., 2010) (Experimental Procedures, Extended Experimental Procedures, and Figure S1B). This enabled us to observe GNPs of 40 nm in diameter with a spatio-temporal resolution of 2 nm and 37 μs (27,000 frames/s; roll-off time = 0.4 ms). The velocity and run length for 40 nm GNP labeled myosin VI were similar to those for TMR labeled myosin VI (Table S1), indicating no significant steric hindrance by the GNP.

Figure 5A shows the time trajectory of movement by such a single myosin VI head. Observed steps were similar to those observed by Qdot labeled myosin. Furthermore, we observed large fluctuations for 30 ms before the plateaus (Figure S3), of which the SD was 2-fold greater than that after the plateaus. These large fluctuations are likely due to Brownian motion by the trailing head when detached from actin. Within each step, there existed two substeps (Figure 5B), the distributions of which are shown in Figure 5C. The first substep had two peaks at 24 nm and 55 nm, while the second substep had only a single peak at 20 nm. To see if the second substep immediately following a small first substep and that following a large first substep are different, we separated them into two groups (second substep following a first substep that was less than 35.5 nm and a first substep larger than 35.5 nm). However, the difference between the two (20 ± 18 nm and 17 ± 15 nm; mean ± SD) was within the deviations and so could not be distinguished. The results indicate that the small (44 nm) step consisted of a 24 nm substep followed by a 20 nm substep, whereas the large (75 nm) step consisted of a 55 nm substep followed by a 20 nm step. Thus, the large and small myosin-VI steps are regulated by the mean position of the first substep.

The Unexpectedly Long and Relatively Rigid Myosin-VI Lever Arms Are Responsible for the Unexpected Large Step

We used these values to speculate the position of the lever arm junction of the leading head while bound to actin. Given that the distance between myosin VI heads just before a step is 36 nm, the lever arm junction should be 19 nm (= 55 nm − 36 nm; see Figures 6A and 6B and "Model for Forward Steps," shown below) anterior to the leading head while bound to actin for a long step, but 12 nm (= 36–24 nm; see Figures 6A′ and 6B′) and "Model for Forward Steps," shown below) posterior for a short step. Thus, the effective lever arm length (19 and 12 nm) is much larger than that (~6 nm) expected from a lever arm consisting of two calmodulin binding domains, 180 degree tilt angle which set the lever arm to be parallel to the actin filament both before and after tilting (Bryant et al., 2007). This then strongly suggests the existence of an unexpected long and relatively rigid lever arm.

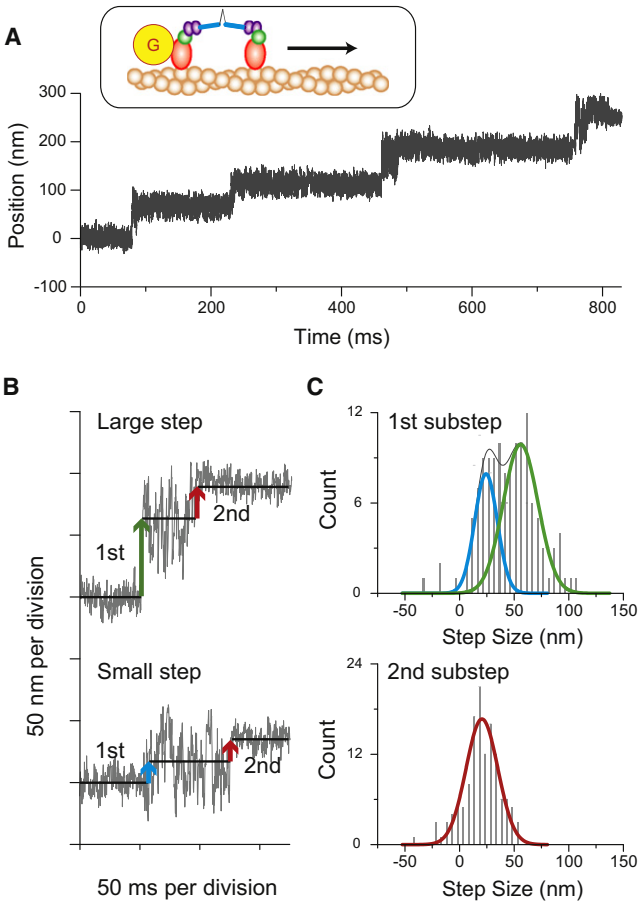

Figure 5. Microsecond NanoImaging of Steps of a GNP-Labeled Myosin-VI Head

(A) Time trajectory of steps by a myosin VI head labeled with a gold nanoparticle (GNP) at 2 mM ATP. Light scattered by GNP was detected with modified dark field microscopy (Figure S1B).

(B) Large and small steps on an expanded time scale reveal an intermediate that corresponds to a one-head bound state. The intermediate breaks the step into two substeps.

(C) Histograms of the 1st and 2nd substep size, respectively. The histogram of the 1st substep size was fit to a two Gaussian function with peaks at 23.8 ± 8.8 and 55.4 ± 14.6 nm, while that of the second substep was fit to a single Gaussian function with a peak at 20.1 ± 12.3 nm. The number of observed steps was 128.

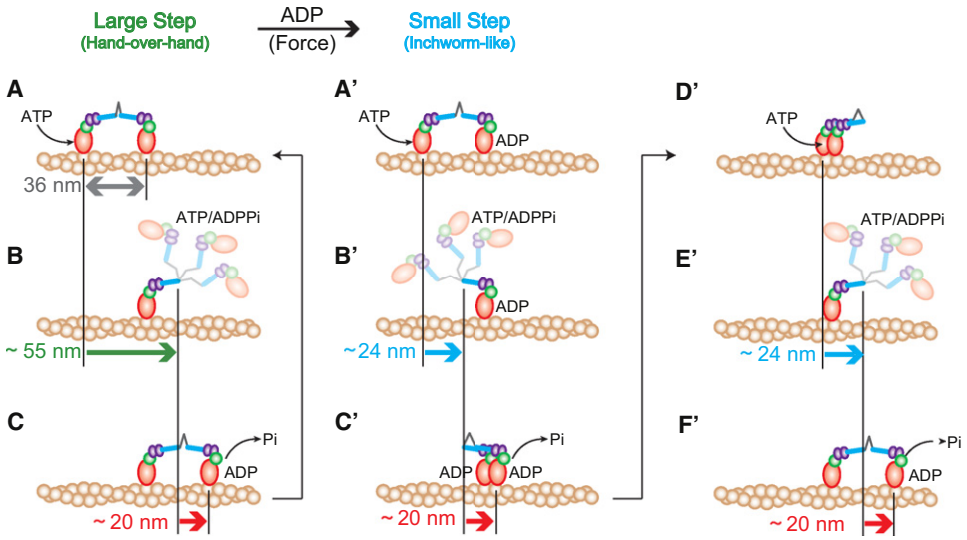

Figure 6. Model for Forward Steps

Left, large hand-over-hand steps; middle and right, small inchworm-like steps. Colors denote the following: N-terminal motor domain (red), the converter domain (green), the lever arm (two calmodulins, purple), the lever arm extension (blue) and the tail domain (black). Green and blue arrows indicate positions of the lever arm junction for large and small steps, respectively. Red arrows indicate the position of the trailing head from the lever arm junction of the leading head when it is bound to actin. The orientations of the lever arms of the two heads in (A) and (A′) are in agreement with a recent report (Mukherjea et al., 2009). In order to explain the effective lever arm lengths, which are 19 and 12 nm for large steps and small steps, respectively, we assume that the position of basal end of the lever arm (green sphere) deviates 3.5 nm toward the pointed end (forward direction) relative to the central axis of the myosin head. This means the lever arm length is 15.5 nm and the 19 and 12 nm effective lever arm lengths are given as 15.5 nm + 3.5 nm and 15.5 − 3.5 nm, respectively. The difference in effective lever arm lengths may be also in part due to the lever arm's flexibility (Spink et al., 2008). See text for details.

We also analyzed the backward step at a high sampling rate, discovering that a backward step also consists of a first substep (−20 nm) and a second substep (−22 nm) (Figure S5). We observed only a single peaked first substep. Therefore, long backward steps of −72 nm are likely prohibited by the mean position of first substep, which is determined by the direction of the lever arm (see "Model for Backward Steps").

DISCUSSION

Numerous single molecule assays have contributed to clarifying the myosin-VI stepping mechanism. This has lead to a prevailing model in which myosin VI moves along an actin filament in a hand-over-hand fashion with a large step size in a manner similar to myosin V, another processive myosin (Nishikawa et al., 2002; Okten et al., 2004; Rock et al., 2001; Yildiz et al., 2004). However, the state of the lever arm during such movement remains controversial. Spink et al. and Sivaramakrishnan and Spudich have proposed that myosin VI extends its lever arm such that it is relatively rigid (Spink et al., 2008 and Sivaramakrishnan and Spudich 2009), whereas Mukherjea et al. suggest this extension leads to a flexible lever arm (Mukherjea et al., 2009). This is an important issue to resolve for explaining how myosin VI generates much larger and more broadly-distributed stepsizes than expected. Here, we conducted nanoimaging of myosin VI steps by monitoring attached Qdots by using FIONA (Yildiz et al., 2003) and SHREC (Churchman et al., 2005) and attached nanogold particles by using TIR dark field microscopy. The results revealed that the large steps were caused by extended lever arms and the broadly-distributed stepsize was due to a mixture of large and small steps of narrow distributions. This led us to propose a model that considers both the hand-over-hand and inchworm models to describe how myosin VI generates and switches its steps, and how this facilitates myosin VI to performing its physiological functions (see below).

Model for Switching between Forward Large and Small Steps

We propose a model for myosin-VI step movement in Figure 6. Forward large steps are described in Figures 6A–6C by a hand-over-hand mechanism: (Figure 6A) both heads first span the actin half helical pitch 36 nm apart; (Figure 6B) the trailing head unbinds from actin upon ATP binding, moves forward 55 nm when the leading head tilts its lever arm, and undergoes Brownian motion; and (Figure 6C) finally binds to the forward actin target 20 nm ahead.

Small forward (44 nm) steps are shown in Figures 6A′–6C′ and 6D′–6F′ in accordance with an inchworm-like mechanism: (Figure 6A′) both heads span the actin half helical pitch 36 nm apart; (Figure 6B′) the trailing head unbinds from actin upon ATP binding, moves forward 24 nm when the lever arm of the leading head remains unchanged, and undergoes Brownian motion; and (Figure 6C′) finally attaches to the forward actin target 20 nm ahead of the leading head. Following this small step, one of the two heads then constitutively undergoes a small forward step (Figures 6D′–6F′) to return to state (Figure 6A′). During the (Figure 6C′) to (Figure 6D′) process, two lever arms should move to the forward direction, although this was not

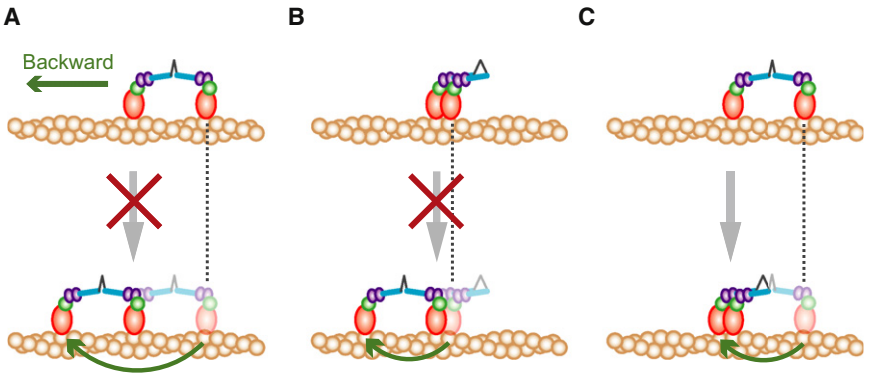

Figure 7. Model for Backward Steps

Colors denote the following: N-terminal motor domain (red), the converter domain (green), the lever arm (two calmodulins, purple), the lever arm extension (blue) and the tail domain (black). Green arrows indicate movement of the detached head during backward steps. Three possible backward step patterns are shown. No backward steps take place in the manner described in either (A) or (B). Backward steps are made by the leading head only when both heads span the actin half helical pitch (36 nm) (C). In Fig. 6, processes (D′) through (F′) occur after Figure 7C to produce the subsequent small step.

directly observed in our measurements. Here, we observed a 36 nm distance between the two heads followed by the rear head taking a small forward step. This is consistent with the inchworm model. However, the small forward step was 44 nm (Figure 2A), suggesting the rear head becomes the lead head, whereas in the inchworm model the rear head is always rear. We, therefore, describe our observations by an inchworm-like model (Figure 6C′).

The frequency of small steps was enhanced by adding 100 μM ADP to either 20 μM or 1020 μM ATP (Figures 2B and 2D). This suggests that ADP binding to the leading head switches the orientation of its lever arm from forward to backward pointing in order to generate small steps. Since ADP affinity for myosin VI increases with backward force (Altman et al., 2004), the backward force is expected to regulate the lever arm orientation of the leading head by modulating ADP binding. The lever arm of the leading head points backward due to the intramolecular strain generated when both heads bind to actin (Figure 6A and Figure 6A′) (Reifenberger et al., 2009). Tilting of the lever arm follows detachment of the trailing head in response to ATP binding (Figure 6B and Figure 6B′).

A crystal structure argues that myosin VI takes its post-power stroke state in the ADP binding state (Menetrey et al., 2008). Although initially this appears to challenge our assumption that ADP binding stabilizes the pre-power stroke state, it is important to emphasize that we also assume that the myosin VI-ADP state described in Figure 6B′ and Figure 6C′) is an intermediate state (M′-ADP), similar to the pre-powerstroke state formed just after Pi releases from myosin II in muscle (Goldman, 1987). This is in contrast to the myosinVI-ADP complex crystal structure, which corresponds to the post-powerstroke state (M-ADP).

Overall, our model argues that 1) the tail domain acts as a long and relatively rigid extended lever arm and 2) when the trailing head detaches from actin, the leading head has two conformations in which the lever arm either points forward (tilts), which corresponds to the post-power stroke state, or backward (no tilt), which corresponds to the prepower stroke state. When pointing forward, the trailing head undergoes a large (72 nm) forward step; when pointing backward, the trailing head takes a small (44 nm) forward step. The first point accounts for the large myosin VI step size over a wide range of loads, while the second accounts for the wide distribution of step sizes, which is actually due to two different step types.

Model for Backward Steps

Figure 7 shows three possible explanations for backward steps according to myosin-VI structural information. The large backsteps described in Figure 7A are unlikely because we only observed –42 nm steps (Figure 2A and Figure 4C). The small backsteps described in Figure 7B are also unlikely because SHREC measurements found no backsteps from the adjacent head binding state out of 280 observations. All observed backward steps (155 steps) by SHREC measurements were small and took place only when both heads span the actin half helical (36 nm) (Figure 7C). Since the first substep of a backward step was -20 nm (Figure S5), the lever arm of the trailing head should be directed to the forward direction during backward step generation (Figure 7C). This would prevent −72 nm large backward steps.

Physiological Significance of Switching

Why is switching between large hand-over-hand and small inchworm-like steps important for cellular processes? The large step mechanism is advantageous for transporting vesicles fast and smoothly at low loads. On the other hand, although the small forward and backward steps may constrain effective vesicle transport, they may offer versatility when avoiding obstacles and searching for the correct actin binding sites in a trial and error manner in the crowded cytoskeleton meshwork of a cell (Sivaramakrishnan and Spudich, 2009; Spudich and Sivaramakrishnan, 2010). Furthermore, the adjacent head binding state should be useful for anchoring vesicles or the cell membrane to actin cytoskeletons because any external strain is equally partitioned between the two heads meaning myosin VI can maximize its stall force, which allows it to resist a higher force along the filaments. This is further affirmed by the fact that no consecutive small backward steps were observed. Based on the stepping frequency, we can estimate the force by the adjacent head binding state against backward load. The theoretical energy difference, δu, before and after the backward steps from the ratio of forward and backward steps, Nf/Nb, where Nf indicates the number of small forward steps after the adjacent head binding state and Nb indicates the number of backward steps after the adjacent head binding state, can also be determined. No backward steps were observed (out of 280 observations), i.e., Nb = 0. When Nb = 0, Nf/Nb cannot be calculated. So we assumed Nb = 1 instead, such that Nf/Nb = 280/1 giving

$\delta u = kTln280 = 5.6kT = \sim 23\ nm \cdot pN$. Noting that $F = \delta u/d$, where F is force and d is the characteristic distance (Taniguchi et al., 2005), and assuming d = 44 nm, which approximates a small step, F = ~23 nm pN/44 nm = 0.52 pN. In reality, Nf/Nb and F are larger since Nb < 1 and d < 44 nm. These results mean that the adjacent head binding state can withstand a backward load > 0.52 pN, which suggests this state is ideal when anchoring vesicles inside the cell. Thus, the adjacent head binding state is robust against a backward force. By combining the hand-over-hand and inchworm-like mechanisms, myosin VI should more ably adjust to different environmental conditions, which would then make it more capable of completing its multitude of functions.

EXPERIMENTAL PROCEDURES

Constructs Design and Protein Preparations

To construct myosin VI heavy chain, the Human Myosin VI heavy chain cDNA (Kazusa product ID: KIAA0389) 3′ end from 3064-3856 bp was deleted to obtain a Myosin VI cDNA fragment that encoded amino acids Met^{1}-Ala^{1021}. This fragment included the motor domain, neck domain, and coiled-coil domain. To ensure myosin VI dimerization, chicken gizzard smooth muscle myosin tail gene (3327–4692 bp) encoding Thr^{1109}-Ala^{1564} was obtained from full length cDNA (Accession number X06546: gift from Dr. Ikebe) and added downstream and in frame with the 3′ end of the myosin VI coding sequence via a single alanine. For effective biotin labeling and purification, HaloTag® (DHA, Promega) fragment via a LRRRPTRPAMDPPSK linker and 6 × His-tag fragment were attached at the 5′ end and 3′ end, respectively. For the calmodulin (CaM) construct, the Human CaM coding sequence (Kazusa product ID: ORK11793) was inserted into the pFastBac1 between the BamHI and Hind III sites.

Recombinant viruses for myosin VI heavy chain and CaM were produced by homologous recombination using the Bac-to-Bac Baculovirus Expression System (Invitrogen) into Sf9 cells. After co-infection and incubation for 60 hr, cells were harvested by centrifugation at 6000 × g for 5 min and stored at −80°C.

Frozen cells were suspended and sonicated in 10 mL/g wet cells of lysis solution (20 mM Tris-HCl, pH 8.0, 300 mM NaCl, 0.2 mM EGTA, 5 mM $MgCl_2$, 5 mM ATP, and 10 mM β-mercaptethanol) containing Complete EDTA-Free Protease Inhibitors (Roche Diagnostics). After ultra centrifugation at 10,000 × g for 20 min, soluble fractions were mixed with nickel-charged resin (HIS-Select TM Nickel Affinity Gel, SIGMA) for 1 hr. After the removal of unbound protein, 1 ml of lysis solution and 5 μl of HaloTag PEG-Biotin Ligand (Promega) were added to the resin and incubated at 27°C for 30 min for N terminus biotinylation. Afterward, wash solution (20 mM Tris-HCl, [pH 8.0], 300 mM NaCl, 0.2 mM EGTA, 2 mM $MgCl_2$, 0.2 mM ATP, 10 mM β-mercaptethanol, and 20 mM Imidazole) was added to remove any unreacted reagents. The biotinylated myosin VI was eluted with eluting solution (20 mM Tris-HCl, [pH 8.0], 300 mM NaCl, 0.2 mM EGTA, 2 mM $MgCl_2$, 0.2 mM ATP, 10 mM β-mercaptethanol, and 150 mM Imidazole). Thus, myosin VI was biotinylated at the HaloTag domain attached to the N terminus of its head. Biotinylation was confirmed by using a streptavidin-alkaline phosphatase conjugate and bromochroloindolyl phosphate / nitro blue tetrazolium (BCIP/NBT) as the substrate. All steps were performed at less than 4°C except for the biotinylation reaction.

Myosin-Qdot Conjugation

Qdot525 streptavidin conjugates (Invitrogen) and biotinylated myosin VI were mixed and incubated prior to use for single label experiments and together overnight on ice for double label experiments at a ratio of 1 to 1. *A*ssay *b*uffer (AB; 20 mM HEPES-KOH, [pH 7.8], 25 mM KCl, 5 mM $MgCl_2$, and 1 mM EGTA) was prepared before each experiment. 1 μl Qdot-Myosin VI mixture was diluted 100 × in motility buffer (MB; AB plus an oxygen scavenger system (Harada et al., 1990), ATP regeneration system (Iwaki et al., 2009) and different nucleotide concentrations).

Myosin-Gold Nanoparticle Conjugation

40 nm diameter gold nanoparticles (GNPs, British BioCell International) were resuspended in 30 μl of 2 mM HEPES-KOH, pH 7.8 at a final concentration of 0.9 nM and 2 mg/mL Neutravidin (Invitrogen) and incubated overnight at 4°C. Excess Neutravidin was removed twice by centrifugation at 7400 × g for 2 min in 2 mM HEPES-KOH, (pH 7.8).

Biotinylated myosin VI (~1 μM) was then added to the Neutravidin conjugated GNPs (~0.1 μM) at mixture ratios ranging from 1:1 to 1:10. 0.1% nitrocellulose in n-amyl acetate was added to the flow cell and immediately removed in order to make a thin layer on the coverslip surface. 10 μl α-actinin (1.5 mg/mL in AB) was then added and incubated for 3 min to allow for tight adsorption. Unbound α-actinin was removed by washing with 50 μl AB.

Actin stock was diluted 25 × in AB to 0.4 μg/mL. 10 μl of which was added and incubated for 3 min to allow for tight adsorption. Excess actin was removed by washing with 50 μl AB. The cell was then incubated with 10 μl 5 mg/mL α-casein for 3 min to reduce particle adhesion. Excess α-casein was removed by washing with 50 μl AB. 30 μl MB was then added. Finally, 1 μl GNP conjugated myosin VI solution was diluted 10 × in MB and then added into the flow cell and sealed with nail polish.

Microscopy and Image Analyses

Qdot conjugated myosin VI movement was imaged using total internal reflection fluorescence microscopy (TIRFM) and an Olympus IX71 epifluorescence microscope (Figure S1A). Illumination was provided by a 405 nm laser light (Coherent, Compass405-50CW). The illumination laser was rotated by a Tip-tilt piezo mirror (Physik Instrumente, S-334.2SL) at 30 Hz along the periphery of the objective lens to make an omnidirectional evanescent field in order to prevent interference. The fluorescent photons were collected with a back-illuminated EMCCD camera (Andor, DV887ECS-BV). In the case of the double label experiments, a dual-view apparatus (1 × magnification, Hamamatsu) equipped with dichroic mirrors (DML557 nm, Asahi Spectra) and emission filters (FF01-520/35-25 and FF01-593/40-25, Semrock) was put in front of the camera (Kinosita et al., 1991).

GNP conjugated myosin VI movement was imaged using total internal reflection based dark field microscopy (TIRDFM) (Figure S1B). Illumination was provided by 532 nm laser light (Coherent, Compass 415M). The scattered photons from the GNPs were passed through the center of a perforated mirror and tube lens (Olympus), externally magnified by a TV adaptor (VM2.5×, Nikon) and detected by a high-speed CMOS camera (Photron, FASTCAM-1024PCI).

Image acquisition was performed by commercial software (Andor, SOLIS software). Exported 8 bit data were imported into a custom written program using LabVIEW (National instruments). The spot center for each frame was determined using a double Gaussian fit according to a published method (Thompson et al., 2002; Yildiz et al., 2003, 2004). Accuracy of the spot center detection was 2.0 nm. Images of double labeled myosin were obtained and analyzed in accordance with SHREC (Churchman et al., 2005; Churchman and Spudich, 2007). The fiducial registration error (FRE), which evaluates the accuracy of the control grid function and was used to detect the relative position of the two Qdots (Churchman et al., 2005; Churchman and Spudich, 2007), was 6.3 ± 1.0 nm. To evaluate the stability of the control grid during measurements, we recalculated FRE using the same grid function after two hours, finding no significant change (6.2 ± 0.8 nm), which indicates that the control grid function was sufficiently stable for myosin VI measurements.

For details of the sample preparations for Myosin-Qdot conjugation and Myosin-gold nanoparticle conjugation, microscopy and image analysis, please see Supplemental Experimental procedures.

Finally, all steps were detected by eye.

SUPPLEMENTAL INFORMATION

Supplemental Information includes Extended Experimental Procedures, five figures, and one table and can be found with this article online at doi: 10.1016/j.cell.2010.08.033.

ACKNOWLEDGMENTS

This study is supported by the Ministry of Education, Science, Sports and Culture, Grant-in-Aid for Young Scientists (B), 20770121, 2008-2009 (to S.N.), for Scientific Research on Priority Areas, 60402997, 2007–2008 (to S.N.), by the Yuragi Project of the Japanese Ministry of Education, Culture, Sports, Science and Technology (to T.Y.). We thank member of Yanagida Lab., Noji Lab. and Kinosita Lab. for valuable discussion. We especially thank M.A. Zulliger, R. Iino, K.V. Tabata, S. Sakakihara, S. Furuike; Y. Arai, T. Mimuro-Ichinose and R. Ogawa, for technical help; P. Karagiannis for helpful discussions and comments on the manuscript.

Received: February 27, 2010
Revised: August 5, 2010
Accepted: August 27, 2010
Published: September 16, 2010

REFERENCES

Ali, M.Y., Homma, K., Iwane, A.H., Adachi, K., Itoh, H., Kinosita, K., Jr., Yanagida, T., and Ikebe, M. (2004). Unconstrained steps of myosin VI appear longest among known molecular motors. Biophys. J. *86*, 3804–3810.

Altman, D., Goswami, D., Hasson, T., Spudich, J.A., and Mayor, S. (2007). Precise positioning of myosin VI on endocytic vesicles in vivo. PLoS Biol. *5*, e210.

Altman, D., Sweeney, H.L., and Spudich, J.A. (2004). The mechanism of myosin VI translocation and its load-induced anchoring. Cell *116*, 737–749.

Bahloul, A., Chevreux, G., Wells, A.L., Martin, D., Nolt, J., Yang, Z., Chen, L.Q., Potier, N., Van Dorsselaer, A., Rosenfeld, S., et al. (2004). The unique insert in myosin VI is a structural calcium-calmodulin binding site. Proc. Natl. Acad. Sci. USA *101*, 4787–4792.

Balci, H., Ha, T., Sweeney, H.L., and Selvin, P.R. (2005). Interhead distance measurements in myosin VI via SHRImP support a simplified hand-over-hand model. Biophys. J. *89*, 413–417.

Bryant, Z., Altman, D., and Spudich, J.A. (2007). The power stroke of myosin VI and the basis of reverse directionality. Proc. Natl. Acad. Sci. USA *104*, 772–777.

Churchman, L.S., Okten, Z., Rock, R.S., Dawson, J.F., and Spudich, J.A. (2005). Single molecule high-resolution colocalization of Cy3 and Cy5 attached to macromolecules measures intramolecular distances through time. Proc. Natl. Acad. Sci. USA *102*, 1419–1423.

Churchman, L.S., and Spudich, J.A. (2007). In Colocalization of Fluorescent Probes: Accurate and Precise Registration with Nanometer Resolution. Single-molecule techniques: a Laboratory Manual, P.R. Selvin and T.J. Ha, eds., pp. 73–84.

De La Cruz, E.M., Ostap, E.M., and Sweeney, H.L. (2001). Kinetic mechanism and regulation of myosin VI. J. Biol. Chem. *276*, 32373–32381.

Dunn, A.R., and Spudich, J.A. (2007). Dynamics of the unbound head during myosin V processive translocation. Nat. Struct. Mol. Biol. *14*, 246–248.

Funatsu, T., Harada, Y., Tokunaga, M., Saito, K., and Yanagida, T. (1995). Imaging of single fluorescent molecules and individual ATP turnovers by single myosin molecules in aqueous solution. Nature *374*, 555–559.

Goldman, Y.E. (1987). Kinetics of the Actomyosin ATPase in Muscle Fibers. A Rev Physiol. *49*, 637–654.

Harada, Y., Sakurada, K., Aoki, T., Thomas, D.D., and Yanagida, T. (1990). Mechanochemical coupling in actomyosin energy transduction studied by in vitro movement assay. J. Mol. Biol. *216*, 49–68.

Iwaki, M., Iwane, A.H., Shimokawa, T., Cooke, R., and Yanagida, T. (2009). Brownian search-and-catch mechanism for myosin-VI steps. Nat. Chem. Biol. *5*, 403–405.

Kinosita, K., Jr., Itoh, H., Ishiwata, S., Hirano, K., Nishizaka, T., and Hayakawa, T. (1991). Dual-view microscopy with a single camera: real-time imaging of molecular orientations and calcium. J. Cell Biol. *115*, 67–73.

Lan, G., and Sun, S.X. (2006). Flexible light-chain and helical structure of F-actin explain the movement and step size of myosin-VI. Biophys. J. *91*, 4002–4013.

Menetrey, J., Bahloul, A., Wells, A.L., Yengo, C.M., Morris, C.A., Sweeney, H.L., and Houdusse, A. (2005). The structure of the myosin VI motor reveals the mechanism of directionality reversal. Nature *435*, 779–785.

Menetrey, J., Llinas, P., Cicolari, J., Squires, G., Liu, X., Li, A., Sweeney, H.L., and Houdusse, A. (2008). The post-rigor structure of myosin VI and implications for the recovery stroke. EMBO J. *27*, 244–252.

Mukherjea, M., Llinas, P., Kim, H., Travaglia, M., Safer, D., Menetrey, J., Franzini-Armstrong, C., Selvin, P.R., Houdusse, A., and Sweeney, H.L. (2009). Myosin VI dimerization triggers an unfolding of a three-helix bundle in order to extend its reach. Mol. Cell *35*, 305–315.

Nishikawa, S., Homma, K., Komori, Y., Iwaki, M., Wazawa, T., Hikikoshi Iwane, A., Saito, J., Ikebe, R., Katayama, E., Yanagida, T., et al. (2002). Class VI myosin moves processively along actin filaments backward with large steps. Biochem. Biophys. Res. Commun. *290*, 311–317.

Okten, Z., Churchman, L.S., Rock, R.S., and Spudich, J.A. (2004). Myosin VI walks hand-over-hand along actin. Nat. Struct. Mol. Biol. *11*, 884–887.

Park, H., Li, A., Chen, L.Q., Houdusse, A., Selvin, P.R., and Sweeney, H.L. (2007). The unique insert at the end of the myosin VI motor is the sole determinant of directionality. Proc. Natl. Acad. Sci. USA *104*, 778–783.

Park, H., Ramamurthy, B., Travaglia, M., Safer, D., Chen, L.Q., Franzini-Armstrong, C., Selvin, P.R., and Sweeney, H.L. (2006). Full-length myosin VI dimerizes and moves processively along actin filaments upon monomer clustering. Mol. Cell *21*, 331–336.

Phichith, D., Travaglia, M., Yang, Z., Liu, X., Zong, A.B., Safer, D., and Sweeney, H.L. (2009). Cargo binding induces dimerization of myosin VI. Proc. Natl. Acad. Sci. USA *106*, 17320–17324.

Reifenberger, J.G., Toprak, E., Kim, H., Safer, D., Sweeney, H.L., and Selvin, P.R. (2009). Myosin VI undergoes a 180 degrees power stroke implying an uncoupling of the front lever arm. Proc. Natl. Acad. Sci. USA *106*, 18255–18260.

Rock, R.S., Ramamurthy, B., Dunn, A.R., Beccafico, S., Rami, B.R., Morris, C., Spink, B.J., Franzini-Armstrong, C., Spudich, J.A., and Sweeney, H.L. (2005). A flexible domain is essential for the large step size and processivity of myosin VI. Mol. Cell *17*, 603–609.

Rock, R.S., Rice, S.E., Wells, A.L., Purcell, T.J., Spudich, J.A., and Sweeney, H.L. (2001). Myosin VI is a processive motor with a large step size. Proc. Natl. Acad. Sci. USA *98*, 13655–13659.

Shiroguchi, K., and Kinosita, K., Jr. (2007). Myosin V walks by lever action and Brownian motion. Science *316*, 1208–1212.

Sivaramakrishnan, S., and Spudich, J.A. (2009). Coupled myosin VI motors facilitate unidirectional movement on an F-actin network. J. Cell Biol. *187*, 53–60.

Spink, B.J., Sivaramakrishnan, S., Lipfert, J., Doniach, S., and Spudich, J.A. (2008). Long single α-helical tail domains bridge the gap between structure and function of myosin VI. Nat. Struct. Mol. Biol. *15*, 591–597.

Spudich, J.A., and Sivaramakrishnan, S. (2010). Myosin VI: an innovative motor that challenged the swinging lever arm hypothesis. Nat. Rev. Mol. Cell Biol. *11*, 128–137.

Sun, Y., Schroeder, H.W., 3rd, Beausang, J.F., Homma, K., Ikebe, M., and Goldman, Y.E. (2007). Myosin VI walks "wiggly" on actin with large and variable tilting. Mol. Cell *28*, 954–964.

Sweeney, H.L., and Houdusse, A. (2007). What can myosin VI do in cells? Curr. Opin. Cell Biol. *19*, 57–66.

Taniguchi, Y., Nishiyama, M., Ishii, Y., and Yanagida, T. (2005). Entropy rectifies the Brownian steps of kinesin. Nat. Chem. Biol. *1*, 342–347.

Thompson, R.E., Larson, D.R., and Webb, W.W. (2002). Precise nanometer localization analysis for individual fluorescent probes. Biophys. J. *82*, 2775–2783.

Tokunaga, M., Kitamura, K., Saito, K., Iwane, A.H., and Yanagida, T. (1997). Single molecule imaging of fluorophores and enzymatic reactions achieved by objective-type total internal reflection fluorescence microscopy. Biochem. Biophys. Res. Commun. *235*, 47–53.

Ueno, H., Nishikawa, S., Iino, R., Tabata, K.V., Sakakibara, S., Yanagida, T., and Noji, H. (2010). Simple Dark-Field Microscopy with Nanometer Spatial Precision and Microsecond Temporal Resolution. Biophys. J. *98*, 2014–2023.

Vale, R.D., Funatsu, T., Pierce, D.W., Romberg, L., Harada, Y., and Yanagida, T. (1996). Direct observation of single kinesin molecules moving along microtubules. Nature *380*, 451–453.

Warshaw, D.M., Kennedy, G.G., Work, S.S., Krementsova, E.B., Beck, S., and Trybus, K.M. (2005). Differential Labeling of Myosin V Heads with Quantum Dots Allows Direct Visualization of Hand-Over-Hand Processivity. Biophys. J. *88*, L30–L32.

Wells, A.L., Lin, A.W., Chen, L.Q., Safer, D., Cain, S.M., Hasson, T., Carragher, B.O., Milligan, R.A., and Sweeney, H.L. (1999). Myosin VI is an actin-based motor that moves backwards. Nature *401*, 505–508.

Yildiz, A., Forkey, J.N., McKinney, S.A., Ha, T., Goldman, Y.E., and Selvin, P.R. (2003). Myosin V walks hand-over-hand: single fluorophore imaging with 1.5-nm localization. Science *300*, 2061–2065.

Yildiz, A., Park, H., Safer, D., Yang, Z., Chen, L.Q., Selvin, P.R., and Sweeney, H.L. (2004). Myosin VI steps via a hand-over-hand mechanism with its lever arm undergoing fluctuations when attached to actin. J. Biol. Chem. *279*, 37223–37226.